Dynamic characteristics and hazard analysis of the high-altitude landslide based on multi-source data and numerical simulation

Jingxuan Gao[1,2,3], Xueliang Cui[3,4], Nan Zhang[2]*, Lichao Wang[2], Wenpei Wang[2] and Yuanyuan Li[1]

[1]School of Geological Engineering and Geomatics, Chang'an University, Xi'an, China, [2]China China Institute of Geo-Environment Monitoring, Beijing, China, [3]Gansu Institute of Geo-Environment Monitoring, Lanzhou, China, [4]Observation and Research Station of Geological Disaster in LanZhou, Ministry of Natural Resources, Lanzhou, China

The Bailong River Basin is located on the eastern edge of the Qinghai-Tibet Plateau, where tectonic activities are intense and the geological environment is complex. It is one of the high-incidence areas of high-altitude landslides in China. A total of 316 potential geohazards were identified in the Zhouqu region using the InSAR technique, and their spatial distribution exhibits a clear correlation with regional fault structures. Taking the Lijie landslide as the study subject, this research comprehensively employs high-resolution optical remote sensing, Unmanned Aerial Vehicle (UAV) aerial surveys, *in-situ* monitoring, and numerical simulation techniques to achieve multi-scale, multi-temporal, and three-dimensional monitoring of the landslide, as well as quantitative simulations of its stability and dynamic evolution process. For the significantly deformed A1 and A2 blocks in the Lijie landslide, GNSS and deep displacement monitoring revealed their spatio-temporal deformation characteristics. Numerical simulation indicated that the two deformed blocks were in a critical unstable state under natural conditions (with safety factors of 0.959 and 0.916 respectively), and would easily transform into debris flows after instability, posing a serious threat to the residents and towns downstream. This study established a landslide hazard assessment system from identification, monitoring to simulation prediction, providing a scientific basis for geological hazards assessment in strong tectonic zones.

KEYWORDS

landslide hazards, InSAR, in-situ monitoring, numerical simulation, hazard assessment

1 Introduction

Typical high-altitude and long-runout landslides worldwide are predominantly distributed in regions characterized by intense plate tectonic activity, complex geological structures, and sensitive climatic variations (Yin et al., 2023; Yin et al., 2025; Shugar et al., 2021; Mani et al., 2023; Zhang et al., 2020; Wang et al., 2024). On the Qinghai–Tibet Plateau and its surrounding areas, high-altitude and long-runout geological hazards frequently result in mass casualty

incidents. The Bailong River Basin (BRB) is located in southern Gansu Province, within the western segment of the Qinling Mountains. It lies at the convergence of the Qinghai–Tibet Plateau, the Loess Plateau, and the Sichuan Basin. Tectonically, the region occupies the eastern margin of the deformation zone associated with the Cenozoic India–Asia collision, characterized by intense neotectonic activity (Qi et al., 2021; Chen et al., 2024; Liu et al., 2024). Furthermore, the basin traverses the mid-northern section of China's North–South Seismic Belt, where seismic events occur frequently. The area exhibits pronounced topographic relief, with high mountains, steep slopes, and deeply dissected valleys. Surface materials predominantly consist of loess and thick unconsolidated deposits. The region is ecologically fragile, experiencing concentrated rainfall patterns that often include short-duration, high-intensity storm events. As a result, landslides and debris flows are widely distributed, highly frequent, and exceptionally hazardous across the basin. These factors collectively establish the Bailong River Basin as one of China's major regions with a high incidence of geological hazards. In recent years, numerous catastrophic events have occurred, resulting in varying degrees of losses to human lives and property, such as Zhouqu giant debris flow, Xieliupo landslide, Jiangdingya landslide, and Yahuokou landslide (Cui et al., 2013; 2016; Xiao et al., 2013; Chong et al., 2023; He et al., 2023; Yang et al., 2024; Yin et al., 2024; Gao et al., 2025).

The application of satellite and remote sensing technologies for the investigation and identification of potential geological hazards hazards has increasingly emerged as a significant area of research within the academic community (Wasowski and Bovenga, 2014; Ge et al., 2019; Xu et al., 2019). Technologies such as Interferometric Synthetic Aperture Radar (InSAR), optical remote sensing, airborne or Unmanned Aerial Vehicle (UAV) Light Detection and Ranging (LiDAR), and Global Navigation Satellite System (GNSS) have been extensively utilized in identifying potential geological hazards threats and monitoring deformation (Colesanti and Wasowski, 2006; Zhang et al., 2018; Liu et al., 2021; Liu et al., 2024; Chong et al., 2023; Gao et al., 2023; He et al., 2024; Zeng et al., 2024). Drawing upon the characteristics and advantages of processing methodologies such as phase stacking, Permanent Scatterer Interferometry (PS-InSAR), Short Baseline Set (SBAS) techniques, and Identified Point Target Analysis (IPTA), a preliminary framework for InSAR-based identification technology suitable for diverse regions has been established. When conducting large-scale surveys in mid to high mountainous areas, the Stacking-InSAR technique is typically recommended (Li et al., 2019; Yin et al., 2022a).

Traditional geological survey methods face challenges in systematically revealing the evolutionary mechanisms and potential risks associated with landslides. As a result, numerical simulation techniques have emerged as essential tools for addressing these issues, becoming pivotal instruments in landslide risk analysis and assessment in recent years. Currently, a diverse array of numerical models has been developed and widely utilized to study landslide mechanisms. These include finite element models (FEM), continuum models, discrete element models (DEM), and multi-method coupling models (Evans et al., 2001; Dufresne, 2012; Cagnoli and Piersanti, 2015; Yin et al., 2016; Yin et al., 2022b; Li et al., 2020; Wang et al., 2020; Gardezi et al., 2021; Chong et al., 2023; Gao et al., 2023; Huang et al., 2024; Zhang et al., 2024; Qiang et al., 2025). Each of these approaches demonstrates excellent applicability

and significant research value within the field of geological hazard studies.

This study uses the Lijie Landslide in the Bailong River Basin as a case. By adopting an interdisciplinary research methodology, it systematically undertakes research on the identification, monitoring, and risk assessment of geological hazards. Through the integration of high-resolution optical remote sensing, InSAR technology, UAV aerial surveying, *in-situ* real-time monitoring, and numerical simulation methods, multi-scale and multi-temporal monitoring of both surface and deep deformations of the landslide has been realized. Moreover, a quantitative simulation of its stability and dynamic processes has been conducted. A landslide hazard assessment framework covering identification, monitoring, simulation, and prediction has been established. This framework provides a scientific foundation and technical support for the prevention and control of geological hazards in the strong tectonic region on the eastern margin of the Qinghai-Tibet Plateau.

2 Geological background

Previous extensive research has revealed the geological setting of Zhouqu County (Chong et al., 2023; He et al., 2023; Yang et al., 2024; Yin et al., 2024; Gao et al., 2025), which is situated on the eastern margin of the Qinghai–Tibet Plateau, within the northern segment of the Bailong River Basin, and at the tectonic junction between the western Qinling Mountains and the Minshan Mountains. The region is characterized by a structurally dominated, erosionally modified mountainous landscape. Topographically, it exhibits a general trend of higher elevation in the northwest and lower in the southeast, with altitudes ranging from 1,173 m to 4,504 m, making it one of the most dramatic regions of topographic relief in China.

Geologically, the area is complex and exhibits intense neotectonic activity. Three major fault systems—the Guanggaishan–Dieshan North Fault (GDNF), the Guanggaishan–Dieshan South Fault (GDSF), and the Diebu–Bailongjiang Fault (DBF)—are distributed in parallel, exerting significant control over the development and spatial distribution of geological hazards. The slope geology is structurally intricate, with the dominant lithology consisting of interbedded limestone, phyllite, and slate, exhibiting a banded distribution pattern. Superficial deposits include loess-like soils and unconsolidated slope and alluvial materials (Chen et al., 2024; Gao et al., 2025).Due to the influence of active faulting, the rock mass is highly fractured, resulting in the formation of failure-prone layers susceptible to collapses and landslides. This structural predisposition, combined with the lithological and topographic conditions, provides a conducive environment for the occurrence of geological hazards (Figure 1).

3 Methods

This research employed an interdisciplinary and integrative research methodology to conduct a systematic exploration of landslide risks (Figure 2). Initially, on the basis of a thorough systematic review of the regional geological background in the Zhouqu area, geological hazard identification work was carried out across the entire Zhouqu County. This was achieved
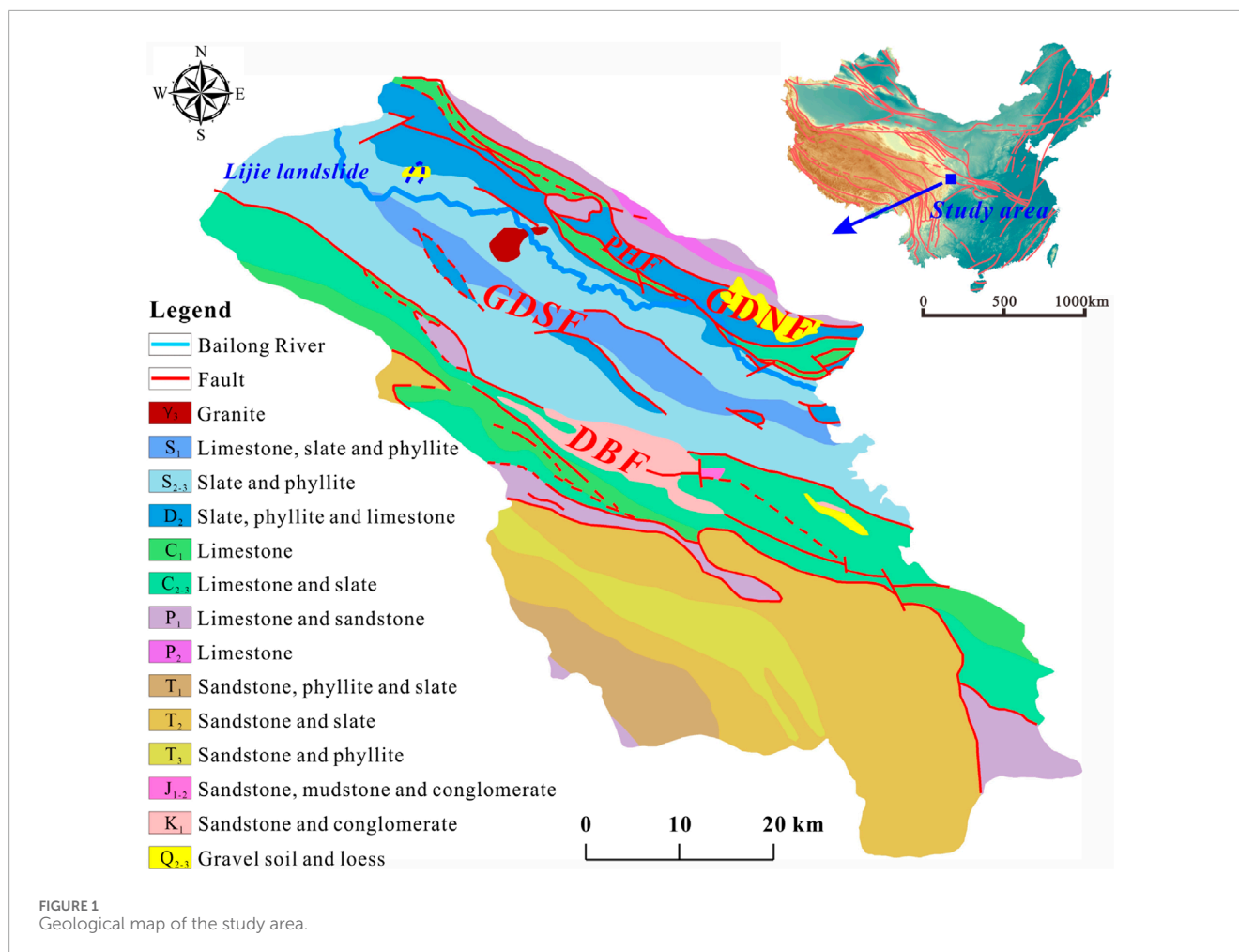
FIGURE 1
Geological map of the study area.

by integrating high-resolution optical remote sensing imagery and InSAR technology. Subsequently, regarding the geological hazard sites posing significant threats within the region, UAV photogrammetry technology and an *in-situ* real-time monitoring system for key deformed areas were utilized to acquire the deformation characteristics of both the surface and subsurface of the landslides. Finally, numerical simulation methods were utilized to quantitatively assess the stability and potential influence scope of typical landslides.

3.1 Geohazards identification

InSAR technology, renowned for its all-weather and continuous operational capabilities, extensive coverage, high spatial resolution, non-contact measurement approach, and low overall cost, demonstrates significant applicability in large-scale geological hazards assessments. The optical image data utilized in this study is sourced from the GF-1 satellite (Figure 3c). Additionally, the high-resolution global digital elevation model (DEM) employed is ASTGTM (ASTER Global Terrain Model), which was collaboratively developed by NASA and Japan's METI based on the processing of optical stereo pairs captured by the ASTER sensor (Figure 3b). Regarding radar remote sensing data, this study

selected C-band synthetic aperture radar (SAR) data provided by the Sentinel-1A satellite. The Sentinel-1 series comprises two C-band radar satellites equipped with a TOPS (Terrain Observation by Progressive Scans) imaging mode that facilitates the acquisition of high-quality and large-scale interferometric phase information (Figure 3d). The swath width in interferometric mode can reach 250 km × 250 km, with a spatial resolution of 5 m × 20 m. This research incorporated a total of 40 ascending orbit Sentinel-1A datasets (Path: 55; Frame: 102) covering the study area within a time span from January 2020 to April 2021. Furthermore, it included 41 descending orbit Sentinel-1A datasets (Path: 62; Frame: 479), spanning from January 2020 to May 2021 (Table 1).

3.2 Integrated investigation approaches

Since January 2021, a systematic and comprehensive investigation has been undertaken on the Liedi Landslide. Firstly, this investigation accurately delineated the boundary of the large-deformation blocks within the landslide mass. Additionally, preliminary assessments were made regarding their developmental characteristics and dynamic evolution trends. By utilizing UAV photogrammetry technology, multiple sets of high-resolution orthophoto imagery data were acquired (Figure 4). Based on these
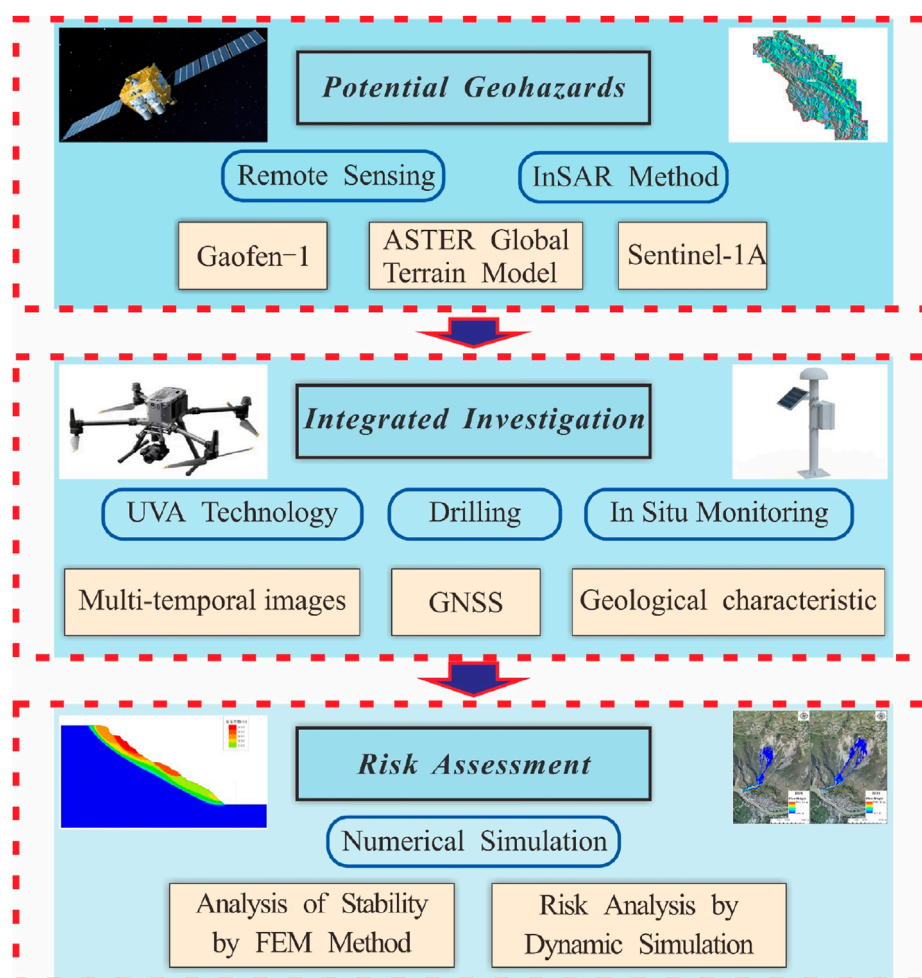
FIGURE 2
Flowchart of the interdisciplinary and integrative methodology in this study.

data, a three-dimensional (3D) model and orthophoto maps of the landslide area were generated. These results provided reliable spatial information to support landslide morphology recognition and deformation monitoring. To further investigate the geological structure of the landslide and analyze the material composition of the sliding mass, drilling surveys were conducted for two major large-deformation blocks. A total of four boreholes were drilled, with core sampling and logging completed (Figure 5a). These efforts yielded crucial geological evidence for an in-depth analysis of the landslide's formation mechanisms and stability evaluation.

3.3 *In situ* real-time monitoring

To elucidate the spatial variation characteristics and temporal evolution patterns of the high-position landslide in Beishan, Lijie, as well as to assess its developmental trends, the research team established a multi-source collaborative deformation monitoring network. Monitoring stations utilizing differential GNSS technology were strategically deployed on two deformation blocks within the landslide mass that exhibit significant current deformation

and an evident trend of instability. Additionally, a benchmark station was established to continuously collect high-precision three-dimensional surface displacement data. By analyzing time-series variations in cumulative displacement and deformation rates at each monitoring point, we can gain a comprehensive understanding of the overall deformation dynamics within the landslide area throughout the monitoring period. Moreover, to thoroughly investigate potential slip surfaces and deep-seated deformation mechanisms, a deep displacement monitoring device was installed in a selected representative borehole. This approach facilitates precise identification of slip zones and enables continuous observation of deep deformation processes. The specific locations of the monitoring points are illustrated in Figure 5a.

3.4 Numerical simulation

The occurrence of landslides fundamentally represents a macroscopic mechanical response to the degradation of internal strength and the adjustment of stress states within the landslide mass. However, traditional geological survey methods
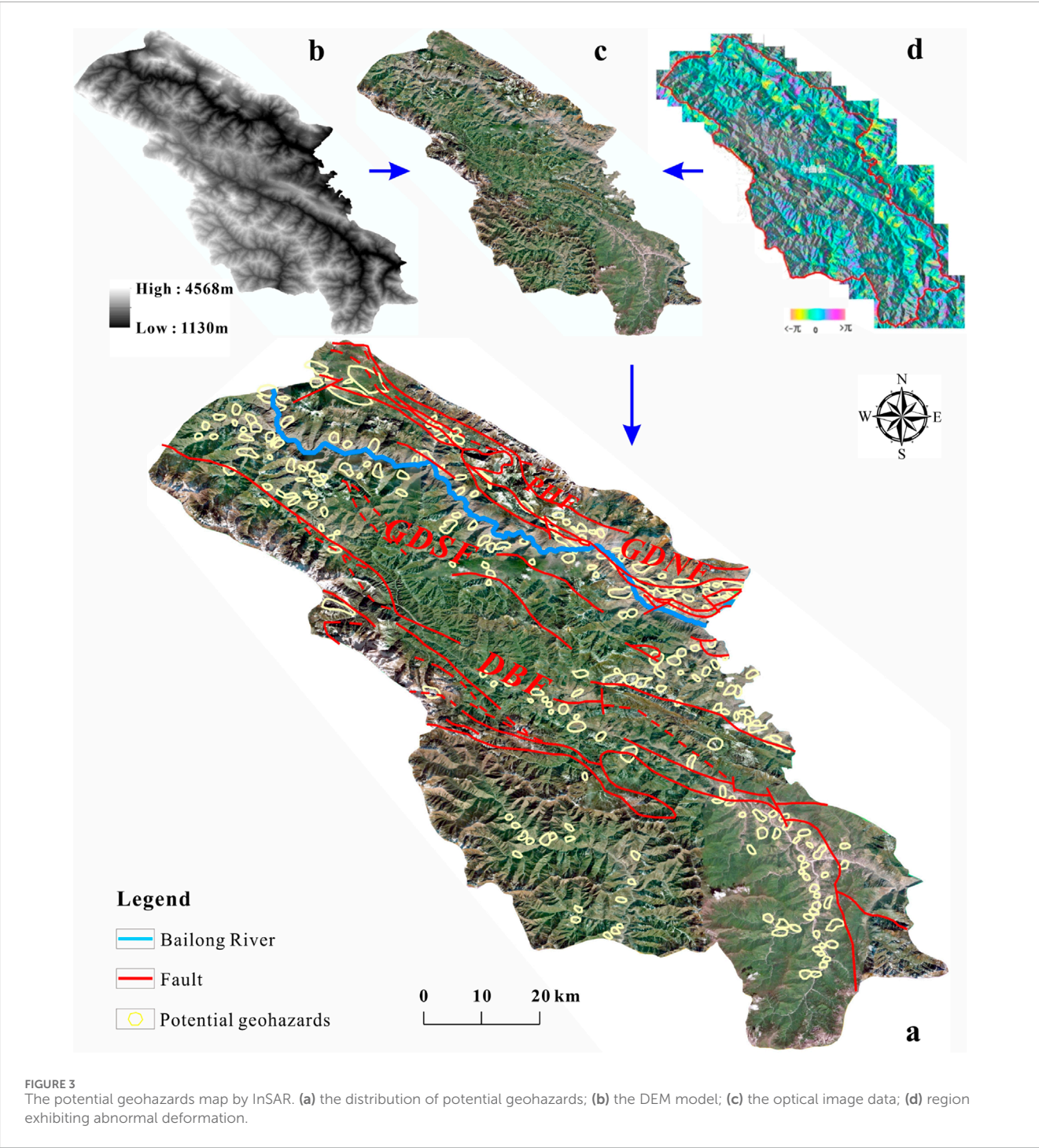
FIGURE 3
The potential geohazards map by InSAR. **(a)** the distribution of potential geohazards; **(b)** the DEM model; **(c)** the optical image data; **(d)** region exhibiting abnormal deformation.

TABLE 1 Parameters for auxiliary data.

Dataset	Source	Resolution
Optical image data	GF-1 satellite	2 m (panchromatic resolution) 8 m (multispectral resolution)
DEM data	ASTER Global Terrain Model	30 m
SAR data	Sentinel-1A satellite	5 × 20 m

FIGURE 4
Historical remote sensing images of the Lijie landslide. **(a)** remote sensing image from Google earth; **(b)** and **(c)** Orthophotos from UAV.
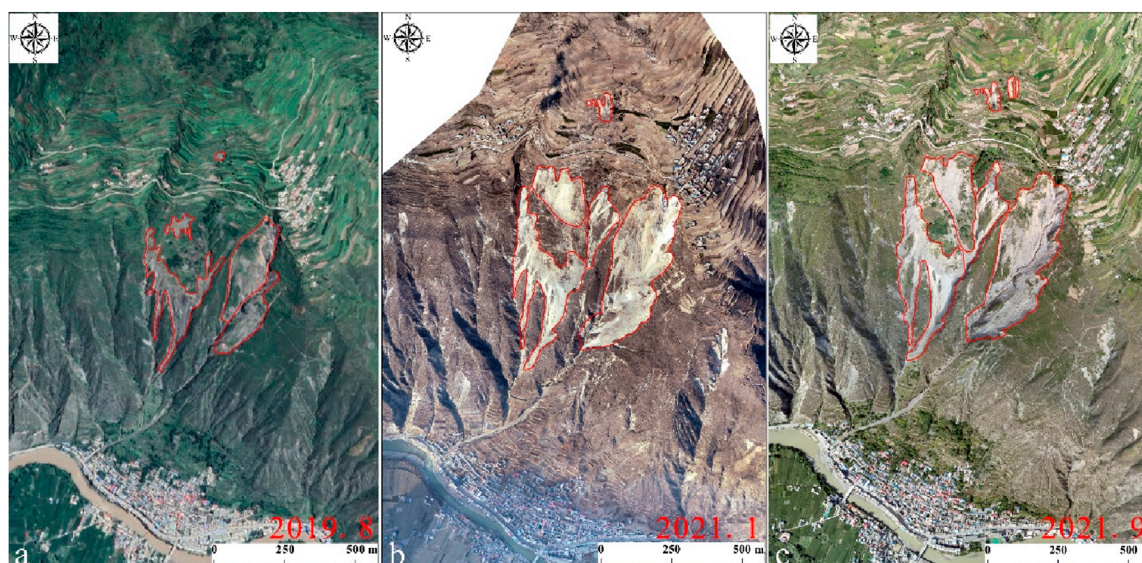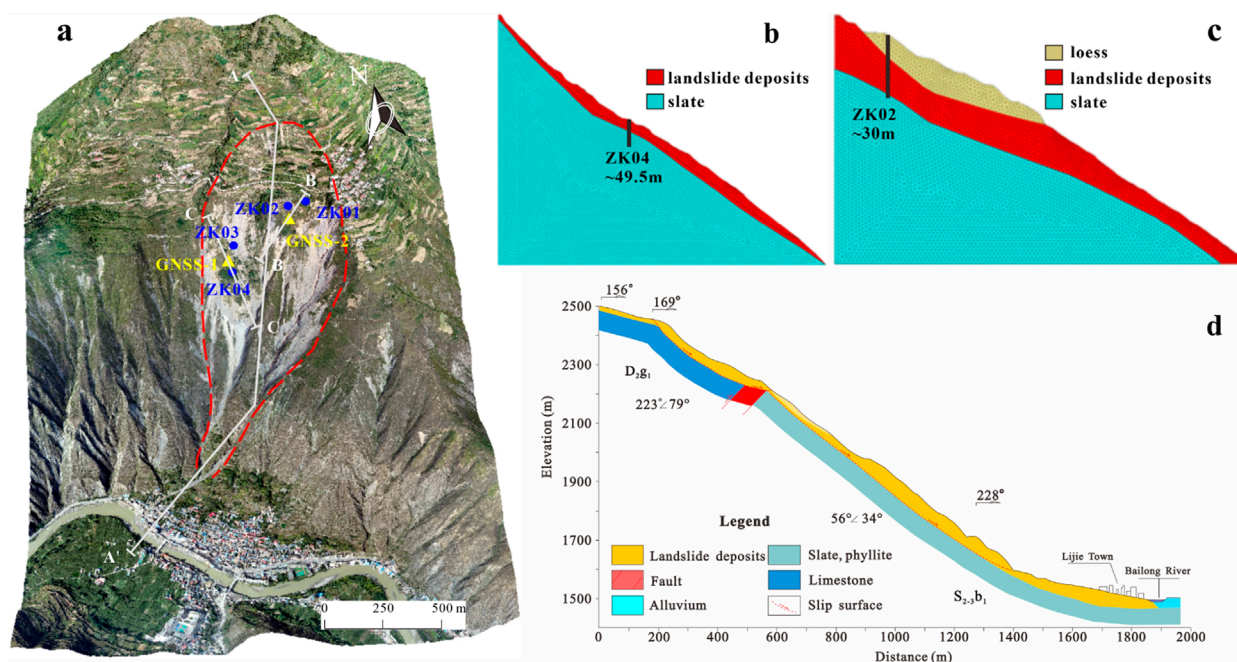

FIGURE 5
Schematic diagram shown boreholes, monitoring points and cross-section. **(a)** Distribution of boreholes and monitoring points. **(b)** The C-C′ cross-section. **(c)** The B-B′ cross-section. **(d)** The A-A′ cross-section.

face significant challenges in comprehensively uncovering the evolutionary laws governing landslide stability and their associated potential risks. These challenges arise from practical constraints during field investigations, the non-visual nature of the internal conditions within rock and soil masses, and the high complexity involved in movement processes following instability. In this context, numerical simulation techniques have emerged as a vital

solution to these issues, becoming essential tools for assessing landslide stability and analyzing related hazards in recent years. This study employed three-dimensional fast Lagrangian analysis of continua (FLAC3D), based on finite difference methods, to simulate both stress-strain behavior and stability characteristics of landslides. Additionally, RAMMS (Rapid Mass Movement Simulation) software—rooted in the Voellmy-Salm rheological

constitutive model—was utilized to simulate movement and deposition processes that occur after landslide instability. This comprehensive approach facilitated a numerical simulation encompassing the entire process from initiation through migration while elucidating underlying mechanisms.

In the process of carrying out the stability numerical simulation research, this study, in combination with the engineering properties of the rock and soil mass at the site and the measurement results of the preliminary laboratory tests, determined the mechanical parameters necessary for the calculation. The unit weight of the landslide deposits was set at 17.5 kN/m^3. The cohesion was 12.7 kPa, and the internal friction angles were 27.5° (the B-B$'$ cross-section Figure 5c) and 20.1° (the C-C$'$ cross-section. Figure 5b) respectively.

In dynamic numerical simulations using the RAMMS software, the Digital Elevation Model (DEM) plays a critical role in terrain construction. The accuracy of the DEM directly impacts the reliability of simulation results. In this study, both the DEM and base map imagery were acquired through UAV aerial surveys, achieving a spatial resolution of 0.5 m. The derived terrain model accurately represents real-world topographic features, meeting the precision requirements for simulating debris flow and mudslide movement processes. Through comparative analysis of remote sensing imagery and detailed field investigations conducted in the preliminary phase of the landslide study, the boundaries of the source area and erosion zone were accurately identified and delineated within the model. The selection and calibration of key parameters—including the dry friction coefficient (μ), the turbulent friction coefficient (ξ), and the erosion coefficient—are crucial for realistically governing debris flow dynamics, as these parameters directly affect the credibility of simulation outcomes (Hungr, 1995). Based on statistical analyses from previous studies on multiple landslide and mudslide events, typical value ranges for μ and ξ are established as 0.05–0.4 and 150–600 m/s^2, respectively. With reference to friction parameter calibration guidelines in the official RAMMS manual and incorporating our research team's simulation experience with cases from the Bailong River basin, we selected μ = 0.23 and ξ = 350 m/s^2 as the optimal parameter set. Detailed values are presented in Table 2.

4 Results

4.1 Geohazards identification results

In this study, the SBAS/Stacking - InSAR technique was employed to monitor and analyze extensive surface deformation. By integrating high-resolution optical remote sensing imagery, a systematic early identification of geological hazards was conducted in the Zhouqu region. A total of 316 potential geological hazard points were identified. On-site field verification confirmed that over 300 of these points were associated with landslide hazards, representing more than 90% of the total identified hazard points (Figure 3). Regarding spatial distribution characteristics, the occurrence of these geological hazards exhibits a significant correlation with fault structures. The majority of hazard points are concentrated along three distinct groups of fault zones. Notably, the highest concentration is observed around the Pingding-Huama

Fault (PHF), which is a branch of the GDNF. This finding aligns closely with previous research results (Qi et al., 2021; Chen et al., 2024; Liu et al., 2024; Yang et al., 2024). Additionally, areas adjacent to the Bailong River are recognized as high-risk zones for geological hazards. Numerous hazardous features such as landslides pose serious threats to both the Bailong River channel and the towns situated along its banks (Figure 3a).

Among the identified potential geological hazards, the Lijie Landslide, located on the left bank of the upper reaches of the Bailong River, represents a significant geological hazard that warrants considerable attention (Figures 4, 6). This landslide has been in a state of creep deformation for an extended period. Historically, various scales of landslides and debris flow events have occurred multiple times in this area. In August 2020, a section of the landslide became unstable due to heavy rainfall conditions and subsequently transformed into a debris flow, obstructing approximately half of the cross-sectional area of the Bailong River channel (Chong et al., 2023; Gao et al., 2025). By January 2021, further developments were observed in relation to this landslide. Numerous cracks and signs of dislocation appeared on the surface of the slope body, resulting in localized deformation as well as damage to roads in Beishan Village, which is situated at mid-slope. Based on onsite investigations and statistical data, this landslide poses a direct threat to both lives and property for approximately 751 individuals residing in nearby towns. The estimated potential economic loss amounts to around 143.38 million RMB. Should there be large-scale instability leading to substantial sliding into the Bailong River, it could trigger a river-blocking disaster that would create a cascading effect characterized by "landslide - river blocking - breach." Consequently, such an event would pose serious risks not only to upstream infrastructure like the Lijie Darong Power Station but also threaten downstream areas including Zhouqu County. The scope and ramifications of such disasters are likely to be immeasurable.
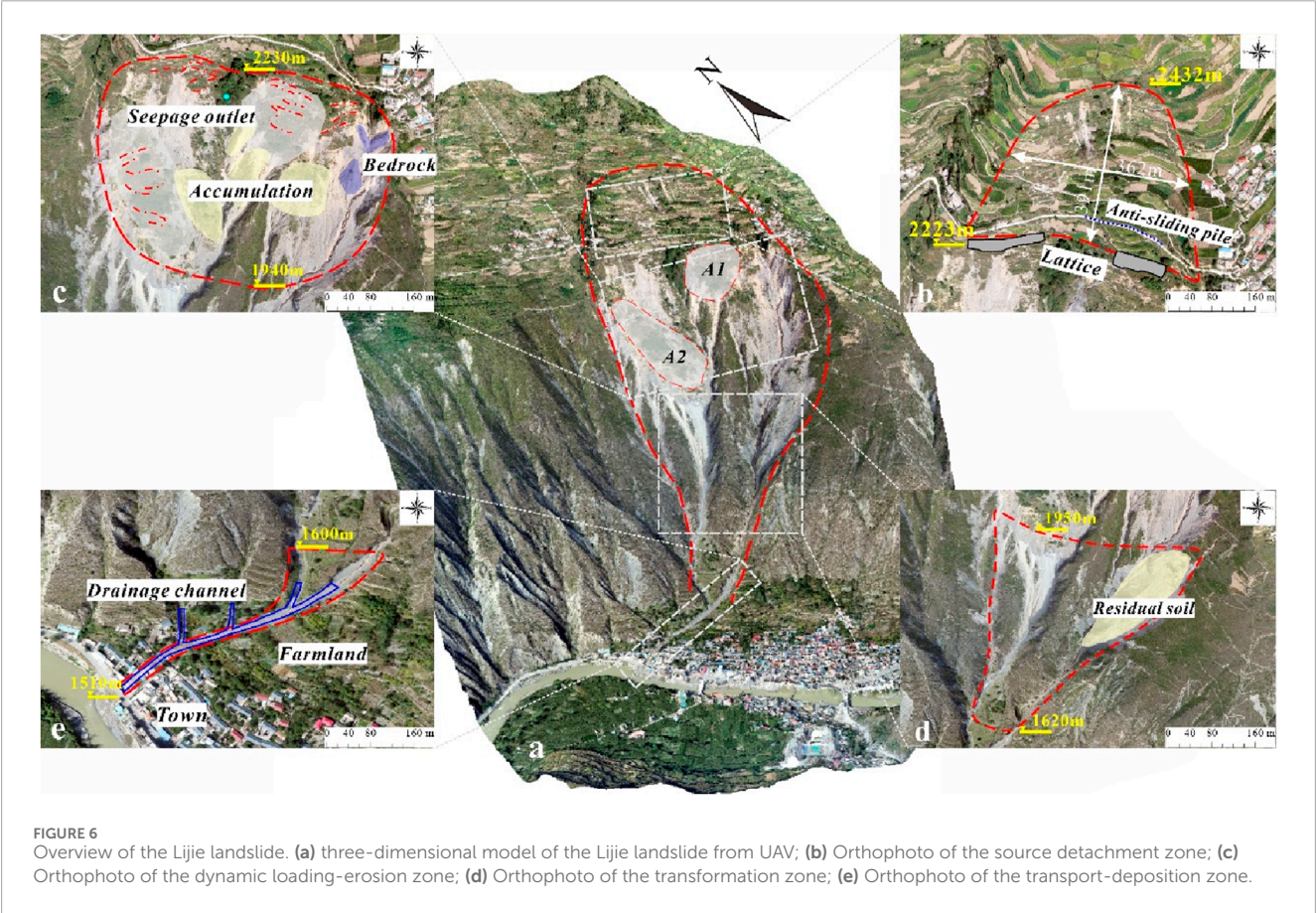
4.2 Integrated investigation results

The Lijie landslide is primarily located within the northern branch fault zone of the Bailong River and the northern margin fault of the Guanggaishan - Dieshan Mountains. This fault represents a significant large-scale regional active fault. Generally, it delineates the geomorphic boundary between the highly uplifted mid-to high-mountain regions and the mid-to low-mountain areas. The terrain within the landslide area exhibits considerable variation. Overall, elevation decreases from north to south. The crest of the northern slope in the source area marks the highest point in this region, reaching an elevation of 2,780 m. Conversely, the lowest point is found at the surface of the Bailong River at the base of this slope, with an elevation of 1510 m. The maximum elevation difference within this landslide area is 1270 m, which typifies a strongly uplifting erosional tectonic landscape characterized by mid- and high-mountain terrains. The average slope measures approximately 35°, while its maximum gradient reaches up to 70°. In general, slopes are inclined towards river valleys (Figures 4, 5d).

The rock strata surrounding the landslide body primarily consist of two sets of ancient formations: the Middle to Upper Silurian Bailongjiang Group and the Middle Devonian Xihanshui

TABLE 2 Simulation parameters.

Model parameters	Resolution	0.5 m
Material parameters	Density	1750 kg/m^3
	Thickness	6 m、4 m
	Volume	7.84 × 10^{4}m^3 (BA1) 9.13 × 10^{4}m^3 (BA2)
	Density of eroded material	1600 kg/m^3
	Cohesion	12.7 kPa
	Internal friction angle	27.5° (BA1) 20.1° (BA2)
	Unit weight	17.5 kN/m^3、
	Elastic modulus	4000 KPa(deposits) 100 MPa(bedrock)
Friction parameters	Erosion rate	0.025 m/s
	μ	0.23
	ξ	350 m/s^2

FIGURE 6
Overview of the Lijie landslide. **(a)** three-dimensional model of the Lijie landslide from UAV; **(b)** Orthophoto of the source detachment zone; **(c)** Orthophoto of the dynamic loading-erosion zone; **(d)** Orthophoto of the transformation zone; **(e)** Orthophoto of the transport-deposition zone.

Group. The remaining layers are predominantly composed of Quaternary soil and gravel deposits. Arranged from older to younger, the lithologies of these strata are as follows: The Middle and Upper Silurian slate and phyllite are exposed in the middle and lower sections of the northern mountain slope, while the Middle Devonian limestone and phyllite can be found in its upper section. Additionally, Late Pleistocene Malan loess from the Quaternary is visible at the upper part of the landslide body as well as on ridges flanking both sides. Furthermore, Holocene secondary loess from the Quaternary, along with slope-deposited gravel soil and landslide-accumulated gravel soil, is extensively distributed throughout the landslide area. Based on a substantial amount of prior research findings (Gao et al., 2025), it has been determined that Lijie landslide represents a high-position shear-out type landslide. In accordance with its deformation characteristics, it can be categorized into four distinct zones when viewed planimetrically: Reactivation-Deformation Zone (Figure 6b), Dynamic Loading-Erosion Zone (Figure 6c), Erosion-Transformation Zone (Figure 6d), and Flow-Accumulation Zone (Figure 6e).

Previously, the blocks exhibiting the most significant deformation within the landslide area were concentrated in the dynamic loading and erosion zone (Figures 4a–c). Influenced by local topography, the loose deposits in this region are undergoing a continuous and progressive disintegration process. This is characterized by multi-stage, block-by-block, and hierarchical failures. Most of the blocks in this area have reached a critical state of instability, with ongoing deformation further exacerbating their precarious condition. Notably, the crack propagation rates of two remaining unstable blocks, A1(BA1) and A2(BA2), have increased markedly, indicating a heightened risk of localized or even widespread collapse. Such deformation behaviors not only pose a severe threat to the overall stability of the Lijie landslide but also present significant potential dangers to the safety of residents in the town below (Figures 4, 6a).

In light of the findings from earlier in-depth on-site investigations, BA1 exhibits an approximately inverted triangular planar configuration. It extends roughly 109 m along the direction of sliding. Influenced by topographical conditions, the width of this block remains relatively uniform, with an average width of around 120 m (Figures 4c, 6a). Numerous cracks have developed on the surface of the block, oriented nearly perpendicular to the principal sliding direction. The lengths of these cracks range between 30 and 100 m, with an average width of approximately 25 cm and an average depth of about 40 cm. In certain localized areas, depression troughs measuring approximately 5–10 cm in depth have already formed. Currently, the deformation and failure mechanisms associated with this block are predominantly characterized by the propagation of tensile cracks at its rear margin and localized slumping at the toe of the slope near its front edge. Based on stratigraphic data obtained from borehole ZK02 (Figure 8), it is evident that the sliding mass primarily consists of clayey gravelly soil, classified as landslide and residual-slope deposits (Figures 7a,c). Vertically, the thickness of this sliding mass gradually decreases from surface level downwards. Horizontally, it displays a spatial distribution pattern where its middle section is thicker while both flanks are thinner. The average thickness of this sliding mass is approximately 6 m, resulting in a total volume estimated at about 7.84×10^4 m^3.

The BA2 exhibits an elongated shape in the planar view, characterized by a broader central section that tapers gradually towards both ends (Figures 4c, 6a). The maximum length of this block along the sliding direction is approximately 173 m, with an average width of 132 m. The slope at the rear edge of this block is relatively gentle, featuring an average gradient of approximately 32°. In contrast, the slopes in the middle and lower sections become significantly steeper, reaching an average gradient of 40°. At this stage, the deformation and failure mode of this block primarily manifest as collapse along the gully at its front edge. To enhance our understanding of the structure of this landslide mass, two boreholes were specifically arranged for investigation. The ZK04 borehole indicated that the landslide mass predominantly consists of loosely structured gravelly soil (Figures 7b,d; Figure 8). Vertically, there is a discernible trend for thickness to increase gradually from the surface downwards. The average thickness measures approximately 4m, while the total volume is estimated to be around 9.13×10^4 m^3.

Comprehensively speaking, the A2 area functions as a relatively independent mass. Its deformation and development are primarily influenced by the high and steep terrain at its leading edge, which exhibits distinct characteristics of traction-type failure. In contrast, the A1 area is affected not only by topographic factors but also by the sliding and pushing actions of the rear-edge landslide mass. This region demonstrates traits indicative of traction-push-type failure. This distinction is fundamentally why the deformation in the BA1 is more pronounced than that in the BA2, with ongoing continuous growth observed.

4.3 *In situ* real-time monitoring results

The BA1 and BA2, where the GNSS-1 and GNSS-2 monitoring points are situated, represent the two areas exhibiting the most intense deformation within the high-altitude landslide zone of Beishan Mountain in Lijie. Influenced by factors such as a significant front-facing overhang and steep terrain, these two blocks have been undergoing continuous downward movement and collapse-type failures. This has led to persistent pull-type rearward expansion deformation, causing the deformation to progressively extend towards the back of the slope. Monitoring data reveals that the deformation rate at the GNSS-1 monitoring point demonstrates an initial trend of rapid increase followed by a gradual decrease. During the phase of rapid deformation, the average rate was approximately 39.7 mm/d, with a peak value reaching 64.4 mm/d; subsequently, this rate eased to an average of about 30 mm/d. Overall, it is evident that BA1 is in a significantly unstable condition: its front edge has experienced multiple collapses and slides; there has been continuous expansion of overhangs; and numerous cracks have developed along both its rear edge and slope surface. These observations indicate that this block is undergoing progressive disintegration and sliding processes. As of 30 September 2021, cumulative displacement at this monitoring point had reached 7,990.3 mm (Figure 9).

The BA2, where the GNSS-2 monitoring point is situated, represents a relatively independent deformation zone. The cumulative displacement recorded at this monitoring point from 3 February 2021, to 30 September 2021, has reached an impressive total of 3,363 mm. The deformation rate remains relatively stable,
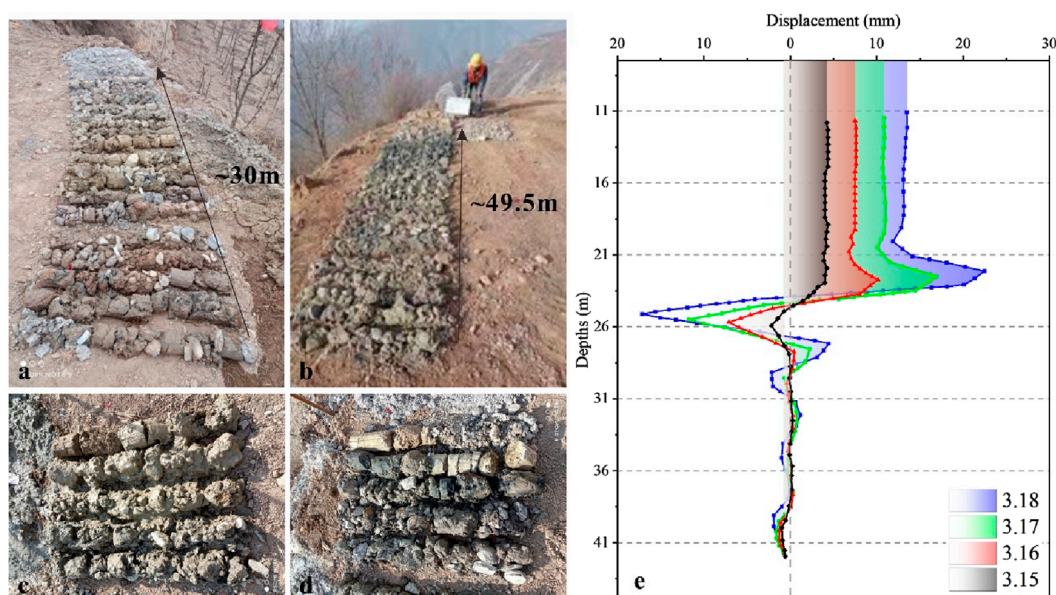
FIGURE 7
The samples from drilling and monitoring curves of deep displacement. **(a)** Samples from ZK02; **(b)** Samples from ZK04; **(c)** and **(d)** The gravelly soil in the slip zone was revealed by drilling. **(e)** Monitoring curves of deep displacement.

exhibiting only minor overall variations in amplitude. The average deformation rate is approximately 18.1 mm/d (Figure 10).

Furthermore, to accurately identify the location of the slip surface and reveal the deep-seated deformation characteristics, this study selected borehole ZK01 for the installation of deep-displacement monitoring equipment. The layout of the monitoring points is illustrated in Figure 5a. The monitoring curves indicate a distinct slip surface at a depth of approximately 23 m behind BA1. At this location, a maximum displacement of around 22 mm was recorded within just 4 days (from March 15th to 18 March 2021, Figure 7e). By integrating the lithological data from the borehole, it can be inferred that this slip surface is situated at the interface between the crushed-stone soil layer and the underlying slate bedrock. Although deep-seated displacement is relatively minor compared to surface displacement, it clearly indicates that the current unstable block is undergoing creep-sliding deformation with overall stability being relatively poor. Presently, deformation is primarily influenced by shallow and loose accumulation bodies. However, the existence of a deep-seated slip surface further substantiates that there exists a potential risk for continuous deformation within this block.

4.4 Numerical simulation results

4.4.1 Numerical simulation results of stability

Figures 11a,b illustrate the horizontal displacement nephogram and vertical displacement nephogram of BA1 under natural conditions, respectively. The findings indicate that displacements are primarily concentrated within the upper accumulation layer of the landslide mass. The maximum horizontal displacement reaches 10.1 m, while the vertical displacement measures 1.7 m. Based on

the distribution of the maximum shear strain increment in the slope mass as depicted in Figure 11c, two potential slip surfaces can be identified. Notably, the most critical slip surface develops within both the residual slope deposit layer and the landslide accumulation body. Its trailing edge penetrates through the landslide accumulation layer and emerges at the leading edge of the residual slope deposit layer. The second potential slip surface is predominantly located within the residual slope deposit layer, extending along the interface between bedrock and overlying strata; it also exhibits characteristics of trailing edge penetration and leading edge emergence. The stability calculation results reveal that BA1 has a safety factor of 0.959, indicating that this section is in an unstable condition under natural scenarios and presents a significant risk for sliding.

The horizontal and vertical displacement nephograms of BA2 under natural conditions are presented in Figures 11d,e, respectively. The results indicate that significant displacements are predominantly concentrated within the upper landslide accumulation body. The maximum horizontal displacement reaches 10.1 m, while the vertical displacement measures 7.5 m. As illustrated in Figure 11f, the distribution of maximum shear strain increments on the slope reveals that the most critical slip surface is situated within the upper landslide deposits. Notably, the rear edge of this slip surface is essentially fully connected, shearing along the interface between the overburden and bedrock at its leading edge. Stability analysis indicates a safety factor of 0.916 for BA2, suggesting that the slope is in an unstable state with a heightened risk of sliding.

4.4.2 Dynamic simulation results

The simulation results indicate that when the BA1 begins to move for a duration of 10 s, the solid source material disintegrates and flows into the two adjacent gullies. Approximately one-fifth of
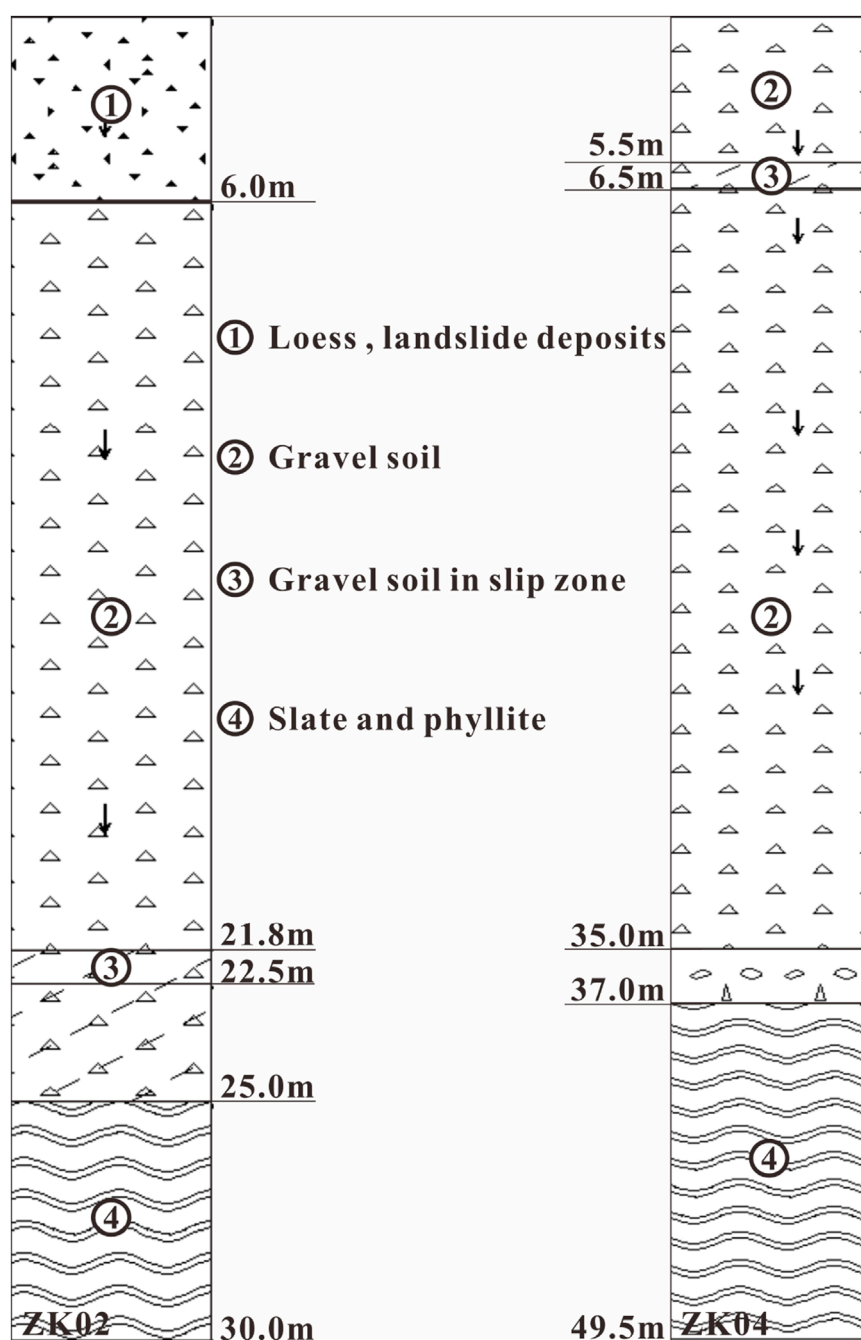
FIGURE 8
The histograms of ZK02 and ZK04.

the source material on the eastern side is influenced by topographical features and enters the eastern gully, while the remaining portion is directed into the western gully. The maximum flow thickness at the leading edge of this mass is measured at 9.65 m, with a peak movement velocity reaching 24.24 m/s. At t = 30 s, all of the source material has been conveyed into their respective gullies. At this juncture, the movement velocity of the leading edge in the western gully attains its maximum value of approximately 26.29 m/s, accompanied by a maximum flow thickness nearing 15.56 m. When t = 50 s elapses, the landslide mass within the western gully reaches what can be termed as a "constriction point." Herein, we observe

a decline in both velocity and an initial accumulation of source material. At this moment, the maximum flow thickness measures around 12.98 m while its peak movement velocity decreases to approximately 22.89 m/s. By t = 75s, portions of this landslide mass have transitioned into drainage channels located at the toe of Beishan landslide. The leading edge's velocity continues to diminish further as accumulation progresses; simultaneously, sections from behind overflow from their confines in western gully and cascade downwards into these drainage channels below. At this stage, we note that maximum flow thickness at where western gully intersects with these drainage channels stands at about 13.02 m; meanwhile some
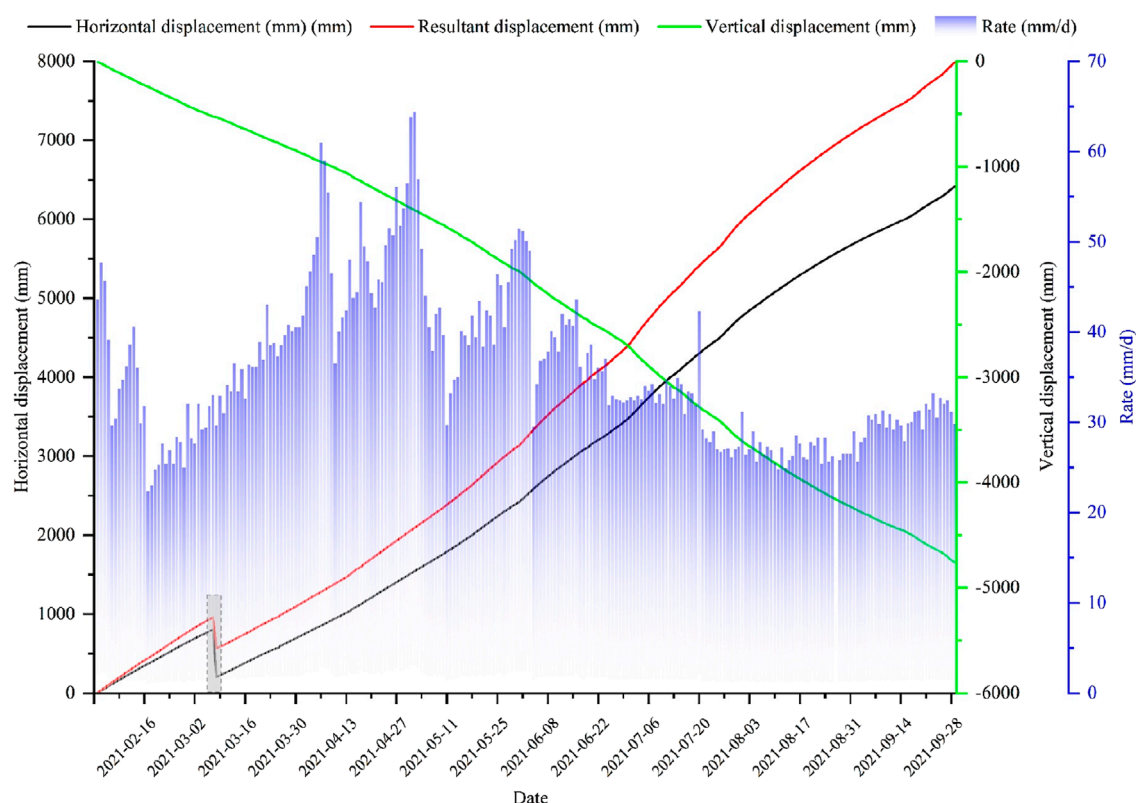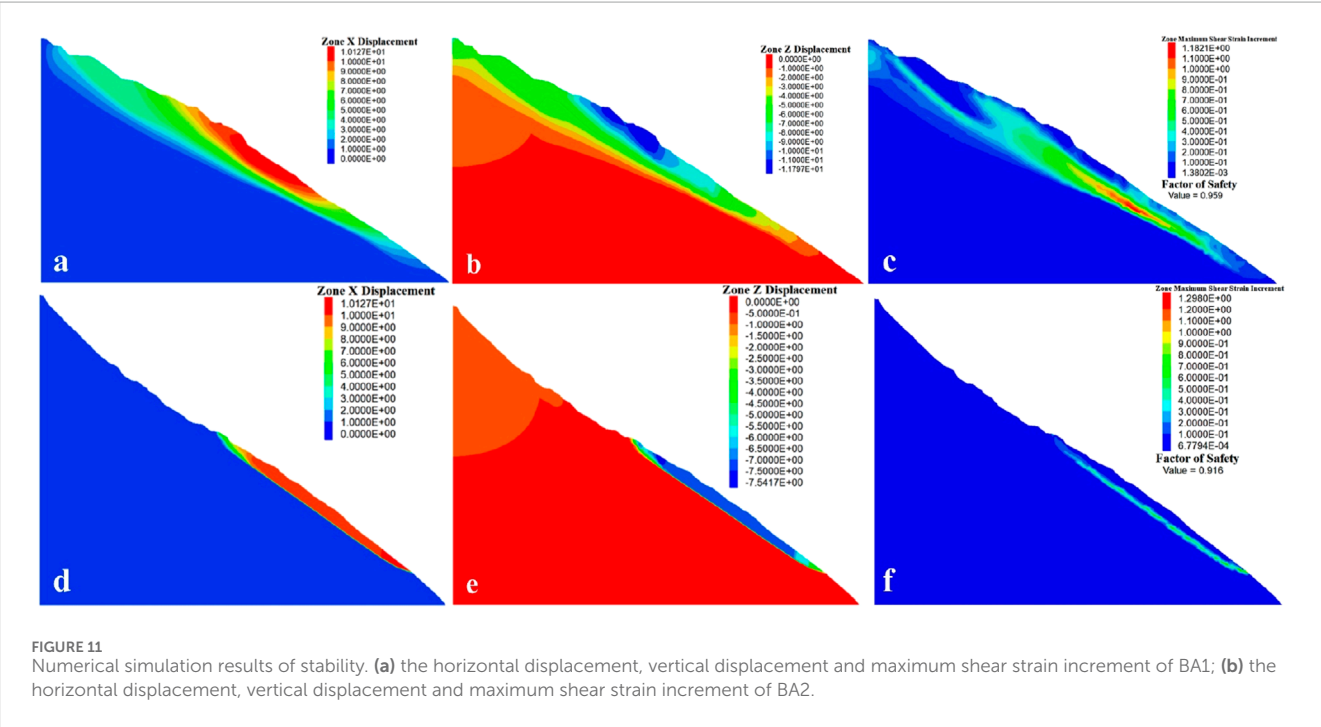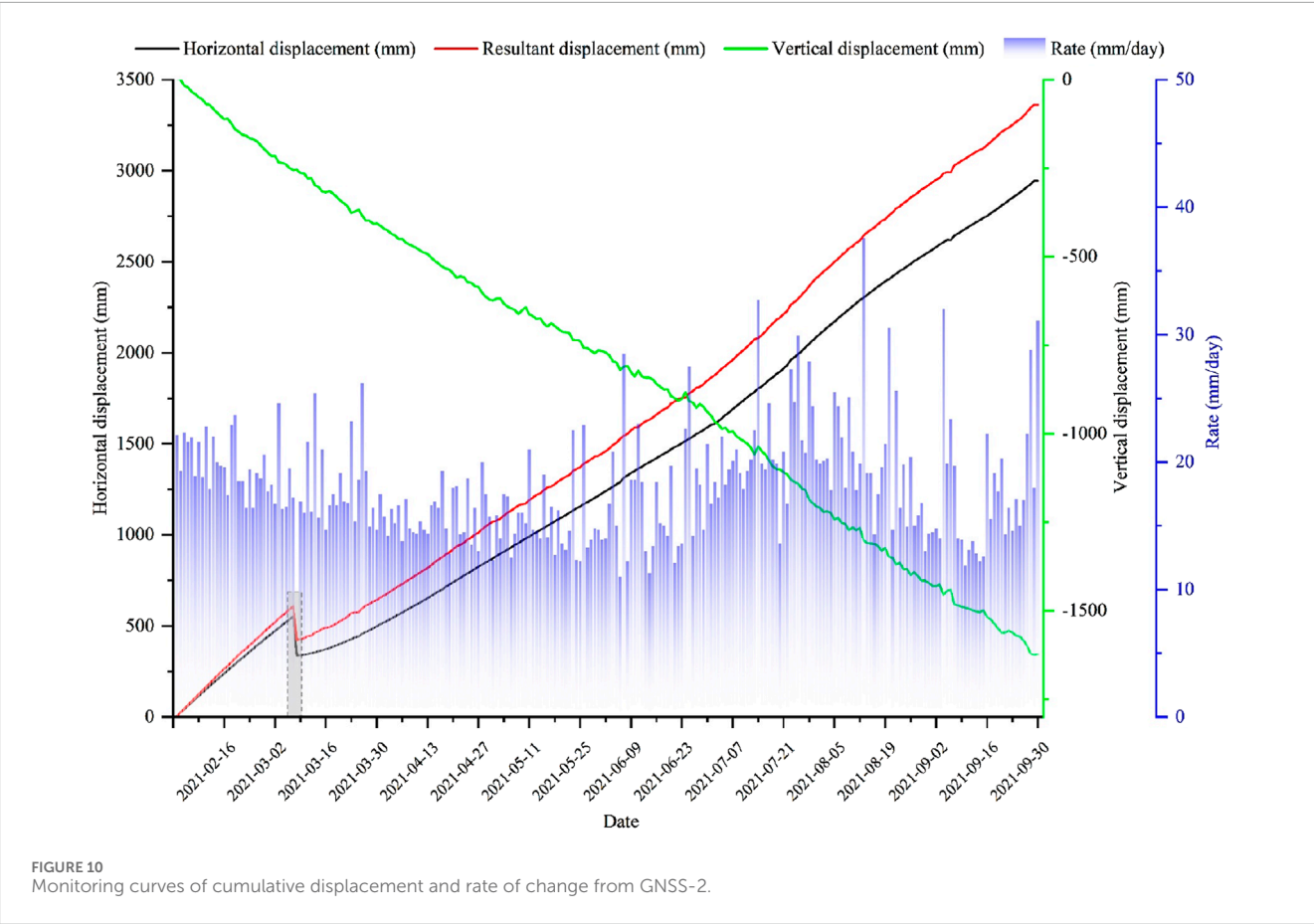
FIGURE 9
Monitoring curves of cumulative displacement and rate of change from GNSS-1.

segments within both eastern and western gullies persist in sliding downward with velocities peaking at around 18.08 m/s. When t = 135 s, although a small amount of source material continued to slide within the gully channel, the main body of the source material had ceased its movement and accumulated within the drainage channel. The maximum accumulation thickness reached 11.2 m, situated at the intersection of the western gully channel and the drainage channel. From the perspective of final accumulation, after the fixed source material in unstable block A1 became entirely unstable and slid downwards, it primarily moved along naturally formed gully channels on the slope. It dispersed and accumulated at the junction of the western gully channel and drainage channel. The accumulation area was predominantly located within the drainage channel at the toe of the slope. A small portion of landslide mass overflowed from this drainage channel, advancing towards a terrace on the eastern side of slope toe. Importantly, it did not directly impact residential areas near the river nor did it flow into Bailong River (Figure 12).

After the initiation of BA2 for a duration of 15 s, the source material of the landslide disintegrated and flowed into the western gully. Approximately one-third of this source material, influenced by the terrain at the western boundary, entered the gully located at the western edge of the slope mass, while the remaining portion flowed into the western gully within the slope mass itself. The maximum flow thickness observed at the leading edge of this mass was 8.76 m, with a peak movement velocity reaching 23.47 m/s. At t = 40 s, all source materials had been directed into two flow gullies on the

western side of the slope mass. At this juncture, the movement velocity at the leading edge of landslide mass in its internal western gully peaked at approximately 26.59 m/s, accompanied by a maximum flow thickness around 10.82 m. By t = 60 s, materials from both western gullies converged at their intersection with a drainage channel. During this period, there was a significant reduction in velocity; specifically, it decreased to about 10 m/s for most parts along with some sections maintaining velocities near 20.02 m/s within that same gully segment. Furthermore, accumulation began to occur from "constriction" points at front end of westward flowing gully towards drainage channel situated at toe of slope; here maximum flow thickness reached approximately 16.91 m. At t = 115 s, the primary source associated with unstable block A2 ceased its motion and became deposited within drainage channel. The maximum accumulation thickness recorded was measured as being 13.79 m, with leading edge deposits having extended up until mouth area surrounding said drainage channel. Based on the results of numerical simulations, it has been observed that following the overall instability and downward movement of the solid sediment source within the BA2, the primary pathway for sediment transport occurs along natural channels formed on the slope. A small portion of the sliding mass comes to rest and accumulates in areas with gentler gradients within these channels. The main sediment source is concentrated at the drainage chute located at the toe of the slope, where it is essentially in a state of siltation. In both the middle and rear sections of the drainage chute, accumulated sliding material overflows from this chute and extends onto the terrace situated
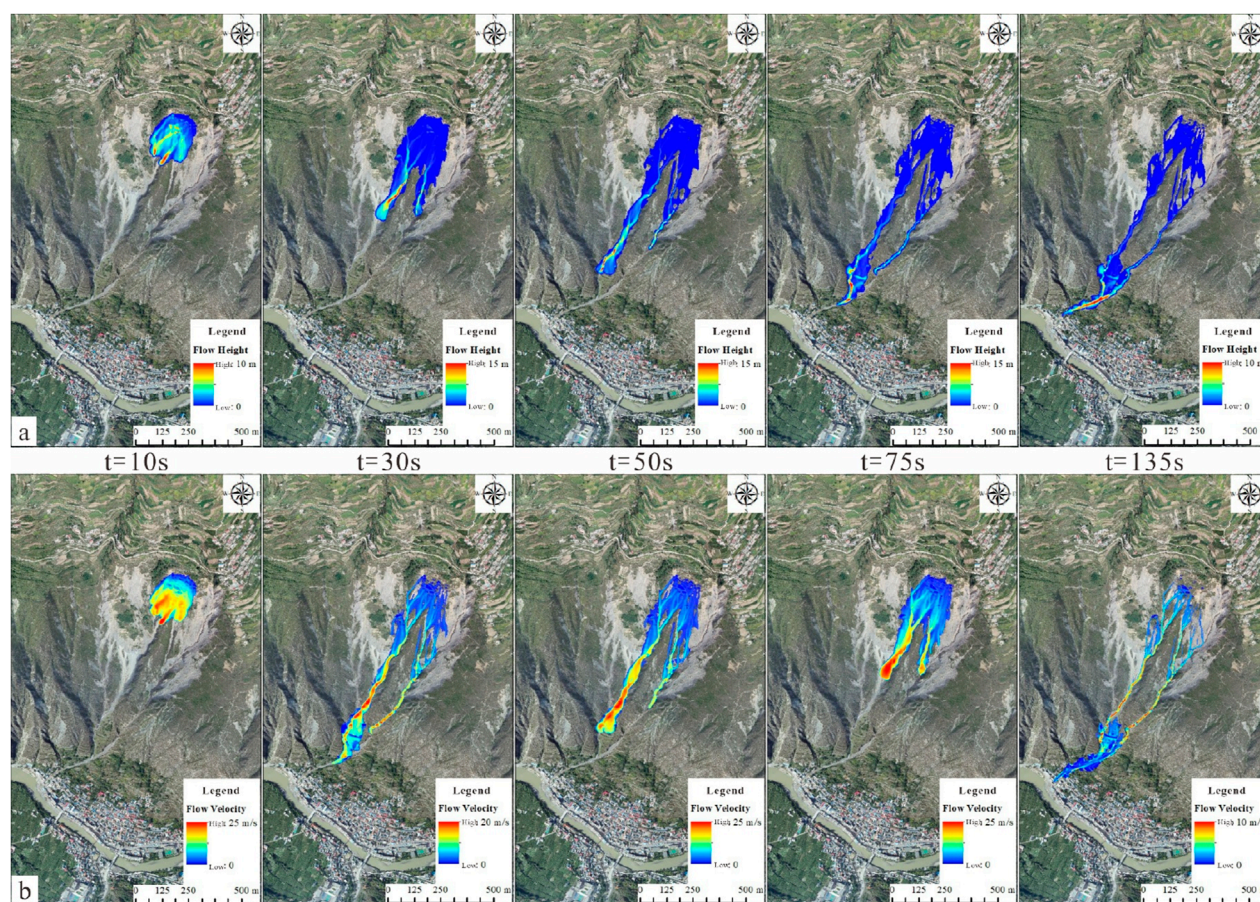
FIGURE 10
Monitoring curves of cumulative displacement and rate of change from GNSS-2.

FIGURE 11
Numerical simulation results of stability. **(a)** the horizontal displacement, vertical displacement and maximum shear strain increment of BA1; **(b)** the horizontal displacement, vertical displacement and maximum shear strain increment of BA2.

FIGURE 12
Schematic diagram of the thickness **(a)** and movement velocity **(b)** of the sliding mass at different times during the instability and sliding of the A1 block.

on the eastern side of its base. The furthest extent of deposition reaches approximately 35 m from the edge of the drainage chute. Furthermore, scattered buildings located at the eastern edge near this section will also be directly affected (Figure 13).

Taking the dynamic characteristics of BA1 within the western gully as a case study, Figure 14 illustrates the simulation results for the maximum velocity, maximum flow thickness, and erosion depth of the sliding mass following its movement. Once the sliding mass becomes unstable and initiates motion, its velocity steadily increases until it reaches a peak of 23 m/s. Subsequently, upon entering the western gully, this velocity begins to decrease. This decline is primarily attributed to the narrow topography of the gully, which constrains the mobility of the sliding mass. Additionally, an important factor that must not be overlooked is that upon contact with loose deposits within the gully, significant erosion and scouring effects occur in relation to the sliding mass; this also contributes to a reduction in its velocity. Following this phase, fluctuations in velocity are observed in response to variations in both curvature and width along different sections of gully topography. When travel distance exceeds 600 m, accumulation at the leading edge of the sliding mass commences; this impedes further movement from subsequent portions of material and causes velocities to drop below 20 m/s. Once substantial accumulation occurs at lower regions within the gully's leading-edge section, velocities for subsequent

segments plummet below 10 m/s. At this juncture, landslide deposit thickness at points near where it exits into lower areas surpasses 10 m. Ultimately, when all components of the sliding mass have settled into place, the primary deposition occurs between where two east-west gullies converge beneath the slope extending towards Lijie gully drainage channel range—with maximum accumulation thickness reaching approximately 11 m.

5 Discussion

In this research, based on light of the deformation and developmental trends observed in the Lijie Landslide, and taking into full consideration the potential chain-like evolution characteristics and disaster amplification effects that may arise following its instability, this study has developed a risk zoning map for the Lijie Landslide. This map delineates various areas and blocks (Figure 15). Through a comprehensive analysis of the overall deformation characteristics and current development trends of this landslide, it has been determined that two blocks, BA1 and BA2, are presently in a critical state with an imminent risk of local or overall instability. Among these, BA1 exhibits the least stability and is predicted to be the first to slide. The instability of BA1 could potentially disturb adjacent BA2, thereby accelerating
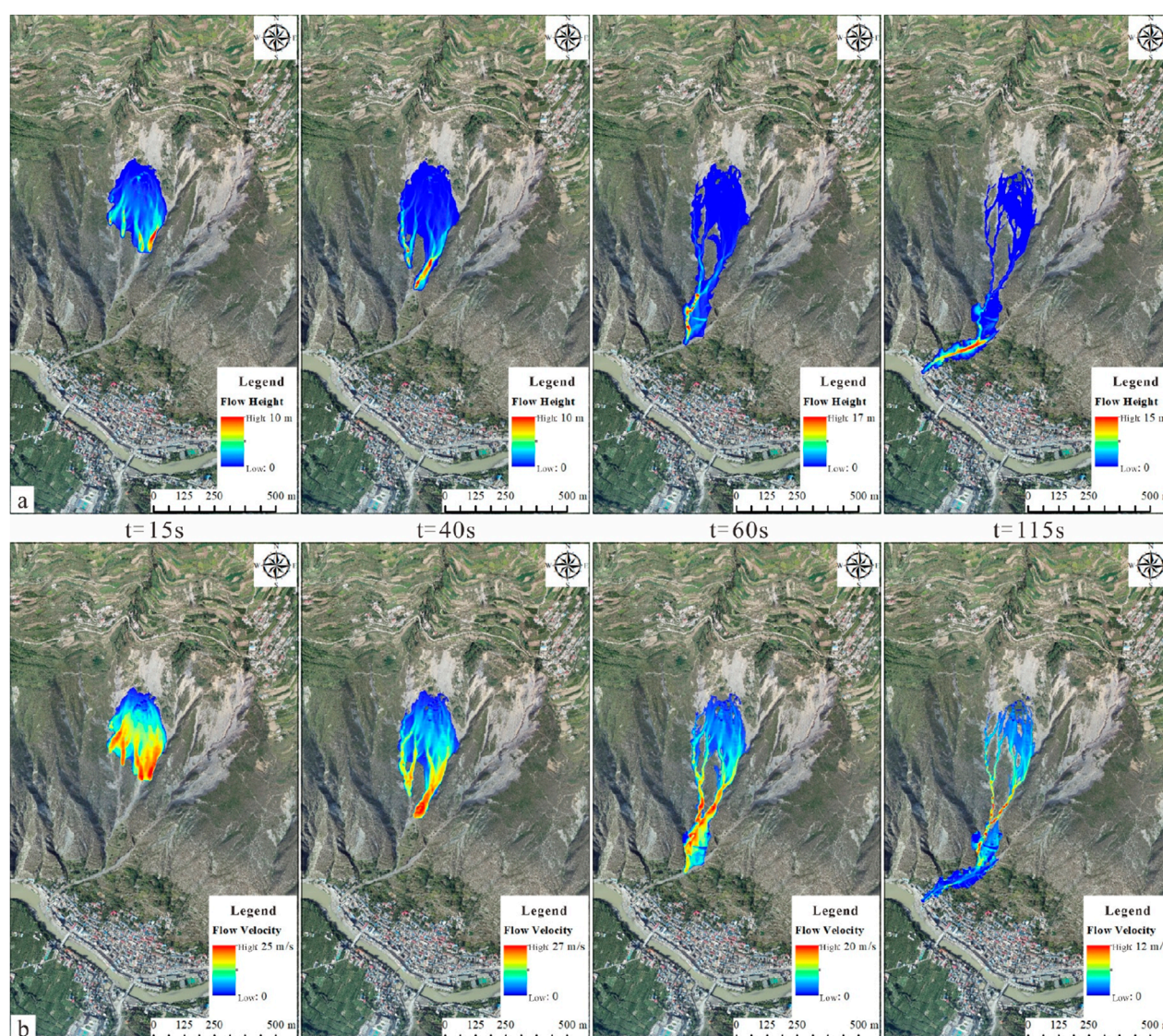
FIGURE 13
Schematic diagram of the thickness **(a)** and movement velocity **(b)** of the sliding mass at different times during the instability and sliding of the A2 block.

its deformation and failure process, which may lead to successive instability in BA2. It is also conceivable that both B A1 and BA2 could slide simultaneously. Should these two blocks become unstable, it would significantly adversely affect the overall stability of the landslide, potentially resulting in a more extensive landslide event. Consequently, it is inferred that the deformation and development of the Lijie Landslide over the forthcoming period may progress through three stages: In stage one, BA1 will experience instability leading to sliding; in stage two, BA2 will either follow suit by becoming unstable or both blocks will slide concurrently; finally, in stage three, there will be an overarching instability affecting the entire landslide. Figure 14 illustrates potential risk influence scopes under different scenarios while providing a scientific basis for disaster risk prevention.

In fact, the use of multi-source data for large-scale regional landslide hazard assessments in the Bailong River Basin has been widely adopted (Chong et al., 2023; Yin et al., 2024; Zeng et al., 2024).

However, limitations in data accuracy and temporal resolution still constrain the effectiveness of these approaches. For landslides characterized by complex structural configurations and deformation behaviors with high potential risks, more detailed and targeted investigations are required. A comprehensive understanding of overall slope stability and hazard potential must be complemented by focused attention on the specific threats posed by individual unstable blocks within the landslide mass. In this study, regarding major potential hazards- Lijie landslide, within the geological structures prone to landslides, further verification was carried out by means of UAV aerial surveys and ground investigations. By deploying a variety of *in-situ* real-time monitoring systems, the spatio-temporal deformation characteristics of the surface and deep parts of the disaster bodies were obtained. This enabled a systematic revelation of their formation mechanisms and evolutionary trends, and the delineation of potential sliding ranges.
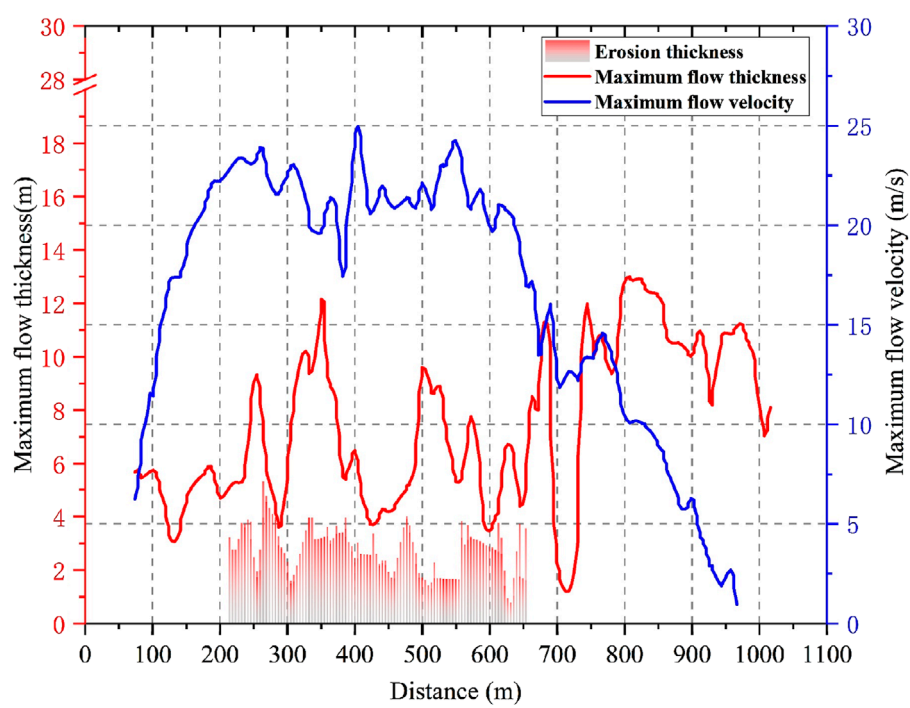
FIGURE 14
Distribution of the maximum velocity, flow thickness, and erosion thickness of the BA1 movement.
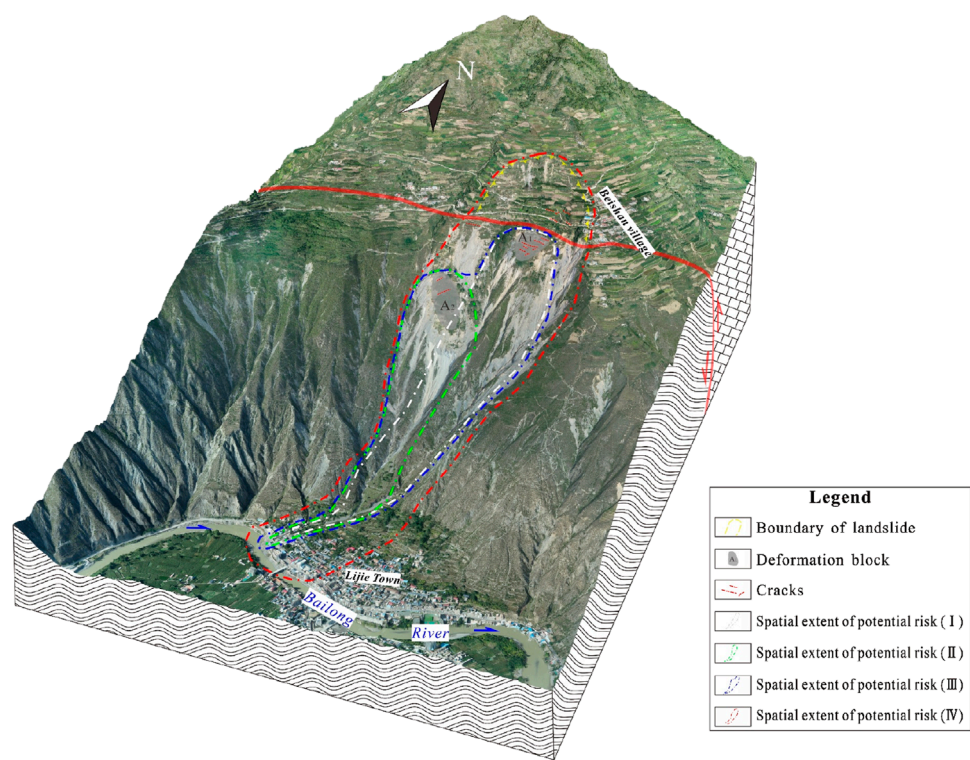

FIGURE 15
The map of potential risks within various blocks. I. The instability-driven sliding of BA1; II. The instability-driven sliding of BA2; III. The instability-driven sliding of BA1 and BA2; IV. The instability-driven sliding of Lijie landslide.

Furthermore, it is particularly important to highlight that the hazard assessment based on the dynamic processes of disasters serves as the foundation and core of the study. To ensure the safety and reliability of this hazard assessment, it is essential to first understand the dynamic characteristics and evolutionary processes of landslides following instability. For instance, through numerical simulation methods, an analysis was conducted on the dynamic behavior of the Lijie Landslide. The results indicate that once initiated by high-position shearing, the landslide exerts impact loading and scouring on loose materials located on both middle and lower slopes as well as within gullies. This phenomenon demonstrates a significant "ploughing effect" along with a volume amplification effect, which subsequently evolves into slope or gully-type debris flows. Such processes considerably enhance the disaster-causing potential associated with landslides. Under rainfall conditions, these debris flows are highly likely to further transform into mudslides.

In conclusion, the research approach integrating multiple disciplines proposed in this paper systematically synthesizes the comprehensive evaluation and dynamic assessment of landslide risks. This can provide scientific references and practical insights for the establishment of a geological hazard risk prevention and control system in the Qinghai-Tibet Plateau and its adjacent regions, especially in the Bailong River Basin.

6 Conclusion

This research employed a comprehensive array of technical methodologies, including remote sensing interpretation, field surveys, *in-situ* monitoring, and numerical simulations, to systematically examine the deformation characteristics, stability, and post-instability dynamic processes of the Lijie Landslide within the Bailong River Basin. The principal findings are as follows:

1. InSAR technology demonstrates significant advantages in the early detection of large-scale geological hazards. In this study, a total of 316 potential geological hazards sites were identified utilizing this technology. Among these, over 300 are classified as landslides. Spatial analysis reveals that the distribution of these disaster sites closely aligns with regional fault structures. This observation underscores the critical role that geological formations play in influencing the occurrence of geological hazards within the Bailong River Basin.
2. Based on an analysis of remote sensing and UAV imagery, combined with *in-situ* three-dimensional monitoring data, it has been determined that the landslide is currently undergoing a continuous creep phase. Among the observed deformations, those of two blocks, A1 and A2, are particularly pronounced. There exists a potential for local or overall instability to occur at any moment.
3. The results of the numerical simulations indicate that the stability factor for both BA1 and BA2 are below 1.0. Following the instability of these blocks, material sources will migrate along existing gullies. Some of this material may flow into the Bailong River, posing a risk of river blockage and demonstrating a significant chain-disaster effect.

4. A landslide risk assessment framework covering identification, monitoring, simulation, and prediction has been established. This framework provides a scientific foundation and technical support for the prevention and control of geological hazards in the strong tectonic region on the eastern margin of the Qinghai-Tibet Plateau.

Data availability statement

The original contributions presented in the study are included in the article/supplementary material, further inquiries can be directed to the corresponding author.

Author contributions

JG: Investigation, Software, Writing – original draft, Writing – review and editing. XC: Methodology, Resources, Software, Writing – original draft. NZ: Methodology, Supervision, Writing – original draft. LW: Methodology, Writing – original draft. WW: Supervision, Writing – original draft. YL: Software, Supervision, Writing – original draft.

Funding

Acknowledgements

Conflict of interest

The authors declare that the research was conducted in the absence of any commercial or financial relationships that could be construed as a potential conflict of interest.

Generative AI statement

The author(s) declare that no Generative AI was used in the creation of this manuscript.

Any alternative text (alt text) provided alongside figures in this article has been generated by Frontiers with the support of artificial intelligence and reasonable efforts have been made to ensure accuracy, including review by the authors wherever possible. If you identify any issues, please contact us.

Publisher's note

All claims expressed in this article are solely those of the authors and do not necessarily represent those of their affiliated organizations, or those of the publisher, the editors and the reviewers. Any product that may be evaluated in this article, or claim that may be made by its manufacturer, is not guaranteed or endorsed by the publisher.

References

Cagnoli, B., and Piersanti, A. (2015). Grain size and flow volume effects on granular flow mobility in numerical simulations: 3-D discrete element modeling of flows of angular rock fragments. *JGR Solid Earth* 120, 2350–2366. doi:10.1002/2014JB011729

Chen, G., Jin, J., Meng, X., Qi, T., Shi, W., Chong, Y., et al. (2024). Influence of tectonic effects on the formation and characteristics of landslide dams on the NE Tibetan Plateau: a case study in the bailong river Basin, China. *Landslides* 21, 2135–2153. doi:10.1007/s10346-024-02273-1

Chong, Y., Chen, G., Meng, X., Bian, S., Huang, F., Lin, L., et al. (2023). Formation mechanism and quantitative risk analysis of the landslide-induced hazard chain by an integrated approach for emergency management: a case study in the Bailong River basin, China. *CATENA* 233, 107522. doi:10.1016/j.catena.2023.107522

Colesanti, C., and Wasowski, J. (2006). Investigating landslides with space-borne synthetic aperture radar (SAR) interferometry. *Eng. Geol.* 88, 173–199. doi:10.1016/j.enggeo.2006.09.013

Cui, P., Zhou, G. G. D., Zhu, X. H., and Zhang, J. Q. (2013). Scale amplification of natural debris flows caused by cascading landslide dam failures. *Geomorphology* 182, 173–189. doi:10.1016/j.geomorph.2012.11.009

Cui, P., Lei, Y., Hu, K., Zhou, G. G. D., Zhu, X., and Chen, H. (2016). Amplification mechanism and hazard analysis for zhouqu giant debris flow. *IJECE* 9, 71–79. doi:10.13101/ijece.9.71

Dufresne, A. (2012). Granular flow experiments on the interaction with stationary runout path materials and comparison to rock avalanche events. *Earth Surf. Process. Landforms* 37, 1527–1541. doi:10.1002/esp.3296

Evans, S. G., Hungr, O., and Clague, J. J. (2001). Dynamics of the 1984 rock avalanche and associated distal debris flow on Mount Cayley, British Columbia, Canada; implications for landslide hazard assessment on dissected volcanoes. *Eng. Geol.* 61, 29–51. doi:10.1016/S0013-7952(00)00118-6

Gao, H., Gao, Y., Li, B., Yin, Y., Yang, C., Wan, J., et al. (2023). The dynamic simulation and potential hazards analysis of the yigong landslide in Tibet, China. *Remote Sens.* 15, 1322. doi:10.3390/rs15051322

Gao, J., Zhang, N., Cui, X., Wang, L., Wang, W., and Li, R. (2025). Deformation characteristics and initiation mechanism of the Lijie landslide, Zhouqu, China. *Front. Earth Sci.* 13, 1603042. doi:10.3389/feart.2025.1603042

Gardezi, H., Bilal, M., Cheng, Q., Xing, A., Zhuang, Y., and Masood, T. (2021). A comparative analysis of attabad landslide on January 4, 2010, using two numerical models. *Nat. Hazards* 107, 519–538. doi:10.1007/s11069-021-04593-0

Ge, D., Dai, K., Guo, Z., and Li, Z. (2019). Early identification of serious geological hazards with integrated remote sensing technologies: thoughts and recommendations. *Geomatics Inf. Sci. Wuhan Univ.* 44 (07), 949–956. (in Chinese with English abstract). doi:10.13203/j.whugis20190094

He, Q., Guo, F., Li, R., Wang, L., Wang, W., Zhang, N., et al. (2023). Characteristics, mobility and dynamic of the Yahuokou flow-like landslide in Zhouqu, Gansu, China. *Landslides* 20, 629–643. doi:10.1007/s10346-022-02000-8

He, K., Luo, G., Xi, C., Liu, B., Hu, X., and Zhou, R. (2024). InSAR-derived predisaster spatio-temporal evolution of a reactivated landslide. *Bull. Eng. Geol. Environ.* 83, 170. doi:10.1007/s10064-024-03661-6

Huang, F., Liu, K., Li, Z., Zhou, X., Zeng, Z., Li, W., et al. (2024). Single landslide risk assessment considering rainfall-induced landslide hazard and the vulnerability of disaster-bearing body. *Geol. J.* 59, 2549–2565. doi:10.1002/gj.4976

Hungr, O. (1995). A model for the runout analysis of rapid flow slides, debris flows, and avalanches. *Can. Geotech. J.* 32, 610–623. doi:10.1139/t95-063

Li, Z., Yu, C., Yu, C., Xiao, R., Chen, L., Luo, H., et al. (2019). Application of satellite radar remote sensing to landslide detection and monitoring: challenges and solutions. *Geomatics Inf. Sci. Wuhan Univ.* 44 (07), 967–979. (in Chinese with English abstract). doi:10.13203/j.whugis20190098

Li, A., Liu, Y., Dai, F., Liu, K., and Wei, M. (2020). Continuum analysis of the structurally controlled displacements for large-scale underground caverns in bedded rock masses. *Tunn. Undergr. Space Technol.* 97, 103288. doi:10.1016/j.tust.2020.103288

Liu, B., He, K., Han, M., Hu, X., Ma, G., and Wu, M. (2021). Application of UAV and GB-SAR in mechanism research and monitoring of Zhonghaicun landslide in Southwest China. *Remote Sens.* 13, 1653. doi:10.3390/rs13091653

Liu, W., Zhang, Y., Meng, X., Wang, A., Li, Y., Su, X., et al. (2024). Forecast volume of potential landslides in alpine-canyon terrain using time-series InSAR technology: a case study in the Bailong River basin, China. *Landslides* 21, 35–51. doi:10.1007/s10346-023-02135-2

Mani, P., Allen, S., Evans, S. G., Kargel, J. S., Mergili, M., Petrakov, D., et al. (2023). Geomorphic process chains in high-mountain Regions—A review and classification approach for natural hazards assessment. *Rev. Geophys.* 61, e2022RG000791. doi:10.1029/2022RG000791

Qi, T., Meng, X., Qing, F., Zhao, Y., Shi, W., Chen, G., et al. (2021). Distribution and characteristics of large landslides in a fault zone: a case study of the NE Qinghai-Tibet Plateau. *Geomorphology* 379, 107592. doi:10.1016/j.geomorph.2021.107592

Qiang, X., Huang, J., Guo, Q., Yang, Z., Wang, B., and Liu, J. (2025). Dynamic evolution and triggering mechanisms of the simutasi peak avalanche in the Chinese tianshan Mountains: a multi-source data fusion approach. *Remote Sens.* 17, 2755. doi:10.3390/rs17162755

Shugar, D. H., Jacquemart, M., Shean, D., Bhushan, S., Upadhyay, K., Sattar, A., et al. (2021). A massive rock and ice avalanche caused the 2021 disaster at Chamoli, Indian Himalaya. *Science* 373, 300–306. doi:10.1126/science.abh4455

Wang, W., Yin, Y., Zhu, S., Wang, L., Zhang, N., and Zhao, R. (2020). Investigation and numerical modeling of the overloading-induced catastrophic rockslide avalanche in Baige, Tibet, China. *Bull. Eng. Geol. Environ.* 79, 1765–1779. doi:10.1007/s10064-019-01664-2

Wang, L., Wang, L., Zhang, W., Meng, X., Liu, S., and Zhu, C. (2024). Time series prediction of reservoir bank landslide failure probability considering the spatial variability of soil properties. *J. Rock Mech. Geotech. Eng.* 16, 3951–3960. doi:10.1016/j.jrmge.2023.11.040

Wasowski, J., and Bovenga, F. (2014). Investigating landslides and unstable slopes with satellite Multi Temporal Interferometry: current issues and future perspectives. *Eng. Geol.* 174, 103–138. doi:10.1016/j.enggeo.2014.03.003

Xiao, H., Luo, Z., Niu, Q., and Chang, J. (2013). The 2010 zhouqu mudflow disaster: possible causes, human contributions, and lessons learned. *Nat. Hazards* 67, 611–625. doi:10.1007/s11069-013-0592-3

Xu, Q., Dong, X., and Li, W. (2019). Integrated space-air-ground early detection, monitoring and warning system for potential catastrophic geohazards. *Geomatics Inf. Sci. Wuhan Univ.* 44 (07), 957–966. (in Chinese with English abstract). doi:10.13203/j.whugis20190088

Yang, L., Zhang, M., Wang, L., Liu, T., Shi, P., Yin, B., et al. (2024). Failure kinematics and mechanisms of the 2019 Yahuokou flow-like landslide along the Pingding-Huama fault in Zhouqu segment. *Eng. Geol.* 332, 107448. doi:10.1016/j.enggeo.2024.107448

Yin, Y., Cheng, Y., Liang, J., and Wang, W. (2016). Heavy-rainfall-induced catastrophic rockslide-debris flow at Sanxicun, Dujiangyan, after the Wenchuan Ms 8.0 earthquake. *Landslides* 13, 9–23. doi:10.1007/s10346-015-0554-9

Yin, Y., Liu, X., Zhao, C., Tomás, R., Zhang, Q., Lu, Z., et al. (2022a). Multi-dimensional and long-term time series monitoring and early warning of landslide hazard with improved cross-platform SAR offset tracking method. *Sci. China Technol. Sci.* 65, 1891–1912. doi:10.1007/s11431-021-2008-6

Yin, Y., Wang, L., Zhang, W., Zhang, Z., Dai, Z., Zhu, C., et al. (2022b). Research on the collapse process of a thick-layer dangerous rock on the reservoir bank. *Bull. Eng. Geol. Environ.* 81, 109. doi:10.1007/s10064-022-02618-x

Yin, Y., Li, B., Gao, Y., Wang, W., Zhang, S., and Zhang, N. (2023). Geostructures, dynamics and risk mitigation of high-altitude and long-runout rockslides. *J. Rock Mech. Geotechnical Eng.* 15, 66–101. doi:10.1016/j.jrmge.2022.11.001

Yin, B., Yin, Y., Zhang, M., Zhang, C., He, Q., and Wang, G. (2024). Active fault control led to the Moli landslide triggered by rainfall on 26 February 2021 in Zhouqu County, Gansu, China. *Landslides* 21, 83–98. doi:10.1007/s10346-023-02175-8

Yin, Y., Zhang, S., Huo, Z., Yang, C., and Chen, F. (2025). Study on the May 28 Birch high-altitude and long-runout ice-rock avalanche in the SwissAlps. *Chin. J. Geol. Hazard Control* 36 (4), 1–14.

Zeng, J., Zhao, Y., Zheng, J., Zhang, Y., Shi, P., Li, Y., et al. (2024). Early identification of River blockage disasters caused by debris flows in the Bailong River Basin, China. *Remote Sens.* 16, 1302. doi:10.3390/rs16071302

Zhang, Y., Meng, X., Jordan, C., Novellino, A., Dijkstra, T., and Chen, G. (2018). Investigating slow-moving landslides in the Zhouqu region of China using InSAR time series. *Landslides* 15, 1299–1315. doi:10.1007/s10346-018-0954-8

Zhang, S., Yin, Y., Hu, X., Wang, W., Zhu, S., Zhang, N., et al. (2020). Initiation mechanism of the Baige landslide on the upper reaches of the Jinsha River, China. *Landslides* 17, 2865–2877. doi:10.1007/s10346-020-01495-3

Zhang, W., Lin, S., Wang, L., Wang, L., Jiang, X., and Wang, S. (2024). A novel creep contact model for rock and its implement in discrete element simulation. *Comput. Geotech.* 167, 106054. doi:10.1016/j.compgeo.2023.106054